In-situ measurement of machining part deflection with Digital Image Correlation

G. Rebergue, B. Blaysat, H. Chanal, E. Duc

To cite this version:

G. Rebergue, B. Blaysat, H. Chanal, E. Duc. In-situ measurement of machining part deflection with Digital Image Correlation. Measurement - Journal of the International Measurement Confederation (IMEKO), 2022, 187, pp.110301. 10.1016/j.measurement.2021.110301 . hal-03576441

In-situ measurement of machining part deflection with Digital Image Correlation

G. Rebergue[a], B. Blaysat[a], H. Chanal[a], E. Duc[a]

[a] *Université Clermont Auvergne, CNRS, SIGMA Clermont, Institut Pascal, F-63000 Clermont-Ferrand, France*

Abstract

In the context of the aeronautics industry, aluminum alloy structural parts are manufactured in several stages, from forming processes and heat treatments to final machining. Some process steps may generate residual stresses. Thus, material removal during machining releases these residual stresses, which induces part deformation. Such deformations can lead to geometric nonconformity of the machined part. It is therefore essential to control this phenomenon. Due to the variability in residual stress distribution in each raw part, the modeling approaches must to be coupled with experimental measurements. This article thus aims to define a reliable experimental technique for measuring in-plane deformation of large aeronautical parts during their machining. The backbone of the technique relies on Digital Image Correlation (DIC), which enables the contactless measurement of part deformation during machining. Moreover, DIC provides a full-field measurement and a direct evaluation of part deformations. This work discusses more specifically problems related to the use of DIC during machining, the latter corresponding to a particularly harsh environment. Indeed, optical systems undergo undesirable movement and metal chips hide areas of the observed part. These unwanted events corrupt the results. In order to control these problems and consistently apply DIC part deformation measurement during machining, specific methods are proposed in this paper. Finally, DIC measurements are performed during the same machining sequence of two parts. The excellent agreement of the two measurements confirms the reliability of the technique. Finally, measurements are discussed, emphasizing the contribution they provide to the machining community.

Keywords: DIC, Global DIC, milling, residual stresses, metal chips.

---

1. Introduction

The increase in air traffic undeniably leads to a boost in the production of aeronautical parts. Although the use of composite materials is becoming increasingly widespread in an aircraft, most of their structural parts remain made of aluminum alloys. Moreover, in the aeronautical context, during conventional manufacturing of an aluminum block, nearly 90% of the volume of material

Preprint submitted to Measurement *September 30, 2021*

is removed [10]. Such material removal represents new challenges for manufacturers because the geometrical quality of the the machined part is of high expectation. Geometrical machined part defects often lead to the scrapping of high added value parts, up to 47 % when considering the manufacturing of thin-walled parts [10].

Sources of inaccuracy are numerous [31, 32] and is often the summation of various phenomena. As example, in the aeronautical context, residual stresses are present in the raw material due to thermal loads or plastic deformations [14] required for reaching their high mechanical performances. These residual stresses are then redistributed during the material removal of machining and lead to an elastic deformation of the part during and after machining. During machining, these deformations, combined with the large size of the workpiece, induce significant displacements and without special attention, these displacements highly contribute in turn to over-cuts or under-cuts in some areas of the part. After machining and unclamping, the release of residual stress leads to deformation of high magnitude. Several studies have already been conducted to determine the origin of residual stresses [42, 48, 21] and their impact during machining [49, 50, 51]. Specific numerical tools have been developed to predict the impact of the reorganization of residual stresses on part deformation during machining [11, 12]. These studies take into account the initial residual stress map, the machining sequence and the clamping of the part. The phenomena involved, are complex and localized. Thus the measurement of displacements induced by the reorganization of residual stresses during machining is essential to improve the simulation-experience dialogue and to validate numerical prediction.

Thoroughly observing and quantifying the behaviour of a part during its machining is necessary for properly studying the modelling of these phenomena. Usually, measurements are performed off-line by probing a few specific points [29, 23, 3]. Other measurement methods exist, but these only provide point-wise measurements of the part. Recently, [44] smartly uses laser sensors to retrieve the workpiece deformation machined by turning. The rotation of the workpiece allows the laser to scan the complete workpiece. To initiate a robust simulation-experience dialogue, full-field measurements appear therefore particularly relevant. Considering the results obtained by the experimental mechanics community [18], the generalization of new kind of instrumentation to the machining community appear promising.

This article focuses on the development of an experimental method for measuring the in-plane displacement fields of a part during its machining. Several full-field measurement methods exist [18, 25], but the constraints of the machining environment quickly led us to use the Digital Image

Correlation method. Since the seminal work of Sutton [41], Digital Image Correlation (DIC) has been the subject of many developments [5, 6, 9, 36, 35, 46, 47] but it is still rarely used in a machine tool context. In this context, most works concern the analysis of the orthogonal cut [40, 28, 16, 20, 2, 22, 27, 4, 52]. In these studies, full-field measurements are performed in order to observe ship formation during a planing operation or during the cutting of a disc or tube. In most cases, the observed surface area is only a few cm^2 and these works focus on the study of chip formation and the cutting phenomena.

The ambition of this paper is the measurement of the behavior of an entire part during its machining. Initial tests were carried out as a prospect in the work of Cerutti [12]. Then, the work [33] investigated methods to calibrate the optical system in the machining context. This allows the proper setting of the measurement mean in order to conduct an accurate measurement of the machined workpiece deformation between two machining steps. The instrumentation with DIC of a machining-tool during part machining requires that two main issues be circumvented: (i) vibrations caused by the machining easily corrupt the measurements; (ii) metal chips hide the surface of interest observed by the camera. Thus, the aim of this paper is to define the principle of this *in-situ* machining part deformation in-plane measurement, to quantify the obtained measurement accuracy and to apply this measurement method to measure the deformation of an application part during its machining.

The first section of this paper introduces the main principles allowing the use of DIC in the machining environment. The second section presents a study case in which the measurement tool is applied. The results obtained are compared to measurements made with a usual and well-defined off-line probing system. Finally, the article is finalized by in-plane measurements of the workpiece during machining.

2. Methods

DIC is used to measure the displacement fields that occurs on a surface of a specimen, by comparing a reference image and a current image of this surface [41]. DIC is conventionally used in experimental mechanics laboratories, where the environment is usually well-controlled. This section presents an extension of the usual DIC measurement tool dedicated to the context of an *in-situ* measurement of the deformation of a part during its machining.

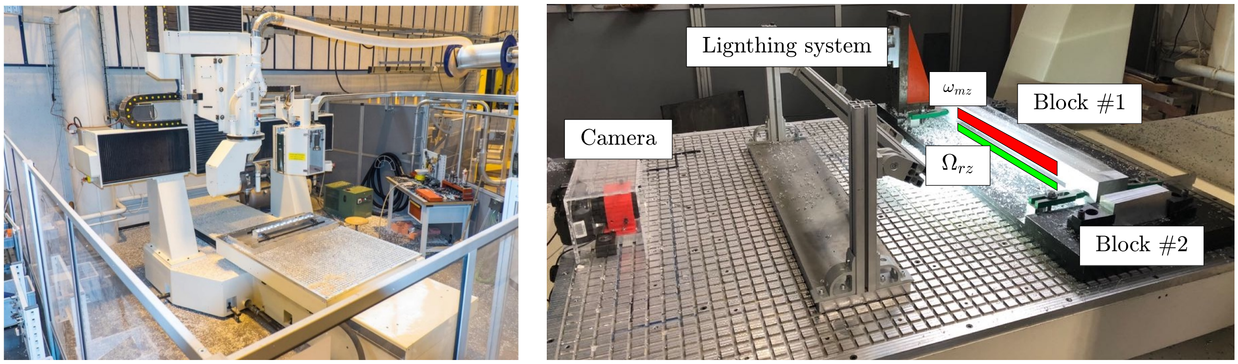

(a) (b)

Figure 1: Illustrations of the CRENO machining-tool (a) and of the experimental set-up (b). The camera, the lightning system and the workpiece (block #1) can be seen in (b). An extra workpiece, denoted Block #2 is also illustrated. This latter is used in the validation procedure proposed in this paper. Two regions of interest ω_{mz} and Ω_{rz} are defined in the imaged area.

2.1. Experimental set-up

In this paper, machining is performed with the machining center CRENO, a 5-axis machine-tool illustrated in Figure 1(a). This machine-tool was chosen because it offers sufficient room for the instruments, and in particular the opportunity to attach the camera to the machining table. The movement along the $\underline{e}_3$-axis is achieved by the table movement. The other two translations are carried out by the gantry ($\underline{e}_1$-axis and $\underline{e}_2$-axis). Finally, the two rotations are located in the spindle. The machine spindle has a maximum power of 12 [kW] and a maximum rotational speed of $24,000$ [rpm]. The workpiece, which is used to illustrate this article, is beam-shaped and made of aluminum alloy 7010.

One side of this workpiece is imaged with a Canon 5DSR reflex camera, featuring a 24×32 [mm^2] CMOS sensor with 50 million pixels. A Tamron 90 macro lens provides a field-of-view of width 404 [mm] with a pixel size of 48 [μm]. Because the distance between the camera and the machined workpiece shall remain constant for consistent DIC measurements, the camera is fastened to the machining table with a specific support, *cf* [33]. Specific attention is paid to ensure the correct locking of the focus of lens during machining whose vibrations might corrupt, *cf* [33]. This is illustrated in Figure 1(b). Table movements and machining vibrations naturally generate loads and impair the data acquisition of the observed surface. The next section highlights this impairment and a strategy is proposed to minimize it. Moreover, metal chips fly in the camera's field-of-view. Thus, the DIC principle, *i.e.* brightness conservation, loses its consistency. An on-line methodology to detect and to define a consistent DIC criterion is then presented.

2.2. DIC adaptation for the machining context

DIC measurements are here performed in the machining environment. Such a harsh constrained environment calls for specialized algorithmic developments in order to ensure consistent measurements. This is the purpose of this section. First, DIC basics are recalled. Further information about the minimization scheme is thus detailed. Next, two dedicated strategies to circumvent measurement impairments caused by the camera movements and flying metal chips are introduced and discussed.

2.2.1. DIC basics

DIC is a numerical method that processes material surface images to retrieve its displacement field. The two images considered here collect the gray level intensities quantified by the camera at times t_1 and t_2. I_{t_1} and I_{t_2} denote the gray level intensities at each pixel location. The imaged surface is assumed to be planar, and its displacement between t_1 and t_2 lies in the same plane. Let $\underline{u}$ be the desired displacement field. For all material points $\underline{m}$ of the imaged region of interest, the displacement $\underline{u}$ satisfies:

$$\underline{m}(t_2) = \underline{m}(t_1) + \underline{u}(\underline{m}(t_1)). \tag{1}$$

Consequently, assuming that the surface texture of each material point remains constant during machining, the gray level intensities I_{t_i} of images at times t_1 and t_2 satisfy, for all pixels $\underline{\mathsf{x}}_{\mathsf{p}}$ in the Region of Interest ω:

$$I_{t_1}(\underline{\mathsf{x}}_{\mathsf{p}}) = I_{t_2}(\underline{\mathsf{x}}_{\mathsf{p}} + \underline{u}(\underline{\mathsf{x}}_{\mathsf{p}})). \tag{2}$$

In practice, many phenomena corrupt this gray conservation law, such as light fluctuations, camera sensor acquisition noise or pixel discretization. A spatial regularization is thus introduced, and the problem is written as a minimization one, over a domain ω. The conventional Sum Squared Difference criterion is implemented here, written as follows:

$$\phi_{t_1}^{t_2}(\omega, \underline{u}) = \sum_{\underline{\mathsf{x}}_{\mathsf{p}} \in \omega} R_{t_1}^{t_2}(\underline{\mathsf{x}}_{\mathsf{p}}, \underline{u})^2 \quad \text{with} \quad R_{t_1}^{t_2}(\underline{\mathsf{x}}_{\mathsf{p}}, \underline{u}) = I_{t_1}(\underline{\mathsf{x}}_{\mathsf{p}}) - I_{t_2}(\underline{\mathsf{x}}_{\mathsf{p}} + \underline{u}(\underline{\mathsf{x}}_{\mathsf{p}})). \tag{3}$$

The residual $\phi_{t_1}^{t_2}$ is then minimized over a kinematic space $\mathcal{U}$ in order to determine the optimal displacement field $\underline{u}^{\mathsf{opti}}$. Usually, the kinematic space $\mathcal{U}$ is elaborated with a set of N shape functions $(\underline{\varphi}_i)_{1 \leq i \leq N}$ defined over ω. The minimization problem is defined as follows:

$$\underline{u}^{\mathsf{opti}} = \sum_{i=1}^{N} a_i^{\mathsf{opti}} \underline{\varphi}_i \quad \text{with} \quad \mathbf{a}^{\mathsf{opti}} = \mathrm{ArgMin}_{\mathbf{a}^* \in \Re^N} \left\{ \phi_{t_1}^{t_2} \left(\omega, \sum_{i=1}^{N} a_i^* \underline{\varphi}_i \right) \right\}. \tag{4}$$

Bold font is used for vectors. Vector $\mathbf{a}$ thus collects the N degrees of freedom a_i, $i \in \{1, ..., N\}$. This problem is incrementally solved. From an initial guess $\mathbf{a}^0$, often chosen as null, the increment $\delta\mathbf{a}^{\mathsf{it}}$ is computed at each iteration it in order to satisfy the stationarity of $\phi_{t_1}^{t_2}$ for $\mathbf{a}^{\mathsf{it}}$. This writes:

$$\mathbf{a}^{\mathsf{it}+1} = \mathbf{a}^{\mathsf{it}} + \delta\mathbf{a}^{\mathsf{it}}, \quad \text{with} \quad \delta\mathbf{a}^{\mathsf{it}} | \forall j \in \{1, ..., N\}, \frac{\partial}{\partial a_j}\left[\phi_{t_1}^{t_2}\left(\omega, \sum_{i=1}^{N}(a_i^{\mathsf{it}} + \delta a_i^{\mathsf{it}})\underline{\varphi}_i\right)\right] = 0. \tag{5}$$

The first term of the Taylor expansion of $\phi_{t_1}^{t_2}$ is considered, and the problem writes:

$$\mathbf{M}^{\mathsf{it}}\delta\mathbf{a}^{\mathsf{it}} = \mathbf{b}^{\mathsf{it}} \quad \text{with} \quad \begin{cases} L_j(\underline{\mathsf{x}}_{\mathsf{p}}, \mathbf{a}^{\mathsf{it}}) = \underline{\nabla I_{t_2}}\left(\underline{\mathsf{x}}_{\mathsf{p}} + \sum_{i=1}^{N} a_i^{\mathsf{it}}\underline{\varphi}_i(\underline{\mathsf{x}}_{\mathsf{p}})\right) \cdot \underline{\varphi}_j(\underline{\mathsf{x}}_{\mathsf{p}}) \\ b_j^{\mathsf{it}} = \sum_{\underline{\mathsf{x}}_{\mathsf{p}} \in \omega} L_j(\underline{\mathsf{x}}_{\mathsf{p}}, \mathbf{a}^{\mathsf{it}}) R_{t_1}^{t_2}(\underline{\mathsf{x}}_{\mathsf{p}}, \sum_{i=1}^{N} a_i^{\mathsf{it}}\underline{\varphi}_i) \\ M_{ij}^{\mathsf{it}} = \sum_{\underline{\mathsf{x}}_{\mathsf{p}} \in \omega} L_j(\underline{\mathsf{x}}_{\mathsf{p}}, \mathbf{a}^{\mathsf{it}}) L_j(\underline{\mathsf{x}}_{\mathsf{p}}, \mathbf{a}^{\mathsf{it}}) \end{cases} . \tag{6}$$

Interested readers can refer to [45, 26] for further information.

In the literature, two main versions of DIC have emerged, *i.e.* the local and global versions. The mathematical formulation of the problem given in Eq.(2) is identical for both versions. Local DIC refers to implementations that rely on small regions of interest ω, called subsets, in combination with a low displacement description $\mathcal{U}$. Only the retrieved displacement of the center of the subset is considered, and the problem is repeated for another subset. The pixel-wise displacement is determined by interpolating the displacement obtained at each subset center. Global DIC, on the other hand, relies on a large region of interest Ω, in which the displacement field $\mathcal{U}$ is defined for describing the kinematics of the whole domain Ω. The next section focuses on the implementation of our proposed methodology , combining both versions of DIC, to correct impairments due to unwanted camera movements.

2.2.2. Strategy for determining and for compensating uncontrolled camera movement

The idea consists in defining two regions of interest ω_{mz} and Ω_{rz} in the camera's field-of-view:

- ω_{mz} corresponds to the measurement zone. It is the workpiece surface whose displacement field needs to be retrieved. From the camera's point of view, this displacement is the composition of the displacement due to deformation mechanisms that occur during material removal, plus the one corresponding to uncontrolled camera movement.

- Ω_{rz} is an imaged zone of the workpiece support and is named the reference zone. This surface remains unaffected during machining and is fixed relative to the machine-tool table. From the camera's point of view and in the absence of camera movement, displacement in this

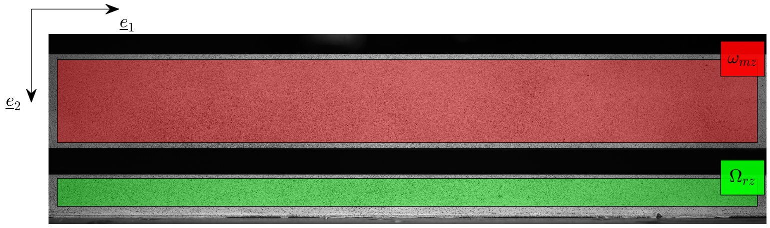

Figure 2: Reference image, which defines the reference state. Two regions of interest are defined here. ω_{mz} is defined on the workpiece surface and corresponds to the measurement zone. A speckle has been painted on this surface. Ω_{rz} is the workpiece support surface, a speckle has also been painted on it.

region of interest shall thus remain null. If displacement is observed in this region, this is the consequence of uncontrolled camera movement.

Figures 1(b) and 2 show these two zones. Particular attention was paid when clamping the workpiece, in order to ensure that the two regions of interest remain in the same plane.

A new DIC criterion Φ^t is consequently defined as follows

$$\Phi^t(\omega_{mz}, \Omega_{rz}, \underline{u}, \underline{u}_{rz}) = \phi^t_{t_0}(\omega_{mz}, \underline{u} + \underline{u}_{rz}) + \phi^t_{t_0}(\Omega_{rz}, \underline{u}_{rz}). \tag{7}$$

where $\underline{u} \in \mathcal{U}$ corresponds to workpiece displacement due to machined material removal. $\underline{u}_{rz} \in \mathcal{U}_{rz}$ reflects the uncontrolled camera movement. Time t_0 corresponds to the initial time of the machining and time t to the time of the current state. Kinematics space $\mathcal{U}$ and $\mathcal{U}_{rz}$ are defined such that :

- *definition of the workpiece kinematic space* $\mathcal{U}$ - the goal here is to avoid the use of any restrictive description for defining the kinematics of a workpiece during its machining. Indeed, any advanced description can also act as a filter. $\mathcal{U}$ is thus defined as the set of low-order polynomial functions, defined on a small domain called subset. In other words, $\underline{u}$ is retrieved using the Local version of DIC. Subsets are squares of size 25×25 pixels. Because illumination is difficult to control in our machining context and also because reflex camera features a high noise-floor, matching functions are 0-order polynomial functions. In the present case study, displacement fields of low spatial frequencies are expected. Measurement is unlikely to be affected by the filtering effect of DIC, this latter being considered as a Savitzky-Golay low-pass filter [37, 17]. In other words, only the subset translations of directions $\underline{e}_1$ and $\underline{e}_2$ are described here;

- *definition of the reference kinematic space* $\mathcal{U}_{rz}$ - Displacements associated with the unwanted camera movements affect the whole images. A global version of DIC is consequently preferred here. Expected displacements are translations of directions $\underline{e}_1$ and $\underline{e}_2$, but also rotation of axis $\underline{e}_3$ and expansion with respect to the $\underline{e}_1$ direction. The hypothesis is taken considering the manner in which the camera is attached to the machining table.

In practice, the determination of displacements $\underline{u}$ and $\underline{u}_{rz}$ are dissociated for reducing the computational cost. $\phi_{t_0}^{t}(\Omega_{rz}, \underline{u}_{rz})$ is indeed first minimized to retrieve $\underline{u}_{rz}$. Then, $\phi_{t_0}^{t}(\omega_{mz}, \underline{u} + \underline{u}_{rz})$ is minimized to retrieve $\underline{u}$.

The proposed strategy is implemented and two specific procedures are performed to validate it. This validation relies on a study of the measurement uncertainty. In these tests, the workpiece is not machined, and the retrieved displacement field shall consequently be null. The measurement here corresponds only to the effect of camera movements or machining vibrations.

The first procedure, denoted here Procedure A, focuses on the influence of movement. It consists in picturing the workpiece without machining. Nevertheless the machine-tool is turned on (the spindle is rotating) and the highest acceleration is assigned to the table to quickly reach $10,000$ [mm/min]. The second procedure, denoted Procedure B, is intended to reproduce the vibrations generated by machining. As illustrated in Figure 1(b), an extra workpiece, denoted Block #2, is clamped to the machining table, close to the observed workpiece, denoted Block #1. In the second procedure, machining is performed on Block #2 while the camera is imaging the surface of Block #1. For each procedure 100 images are acquired. 99 DIC calculations are thus performed using the same reference image for each procedure. Because the purpose is to evaluate the consistency of the measurement in the harsh environment of machining, there is no synchronisation between camera acquisitions and the machining sequence. Consequently, table accelerations or decelerations, but also machining singularities such as the time when the tool enters the material will affect image acquisition and thus impair displacement evaluation. Measurement uncertainties for Procedures A & B without and with uncontrolled camera movement compensation are illustrated in Figure 3. Several remarks can be drawn from these results:

- Considering Procedure A, results are shown in Figure 3(a). The normalized histograms of the raw measured displacement are presented in blue. Red histograms correspond to the measurements obtained with the same set of images but when the proposed strategy for compensating camera movements is applied. For each histogram, the red line highlights the mean data value. The observed workpiece is not machined. The measured displacement shall thus be equal to zero. Camera movements primarily bias the horizontal component of the measured displacement, *i.e.* u_1. Indeed, its average value, denoted here as $\langle u_1 \rangle$, is higher than that of the average value of vertical displacement $\langle u_2 \rangle$ which is almost equal to zero. Moreover, a high dispersion is noticeable in the raw measurements. Figure 3(a) highlights that the proposed

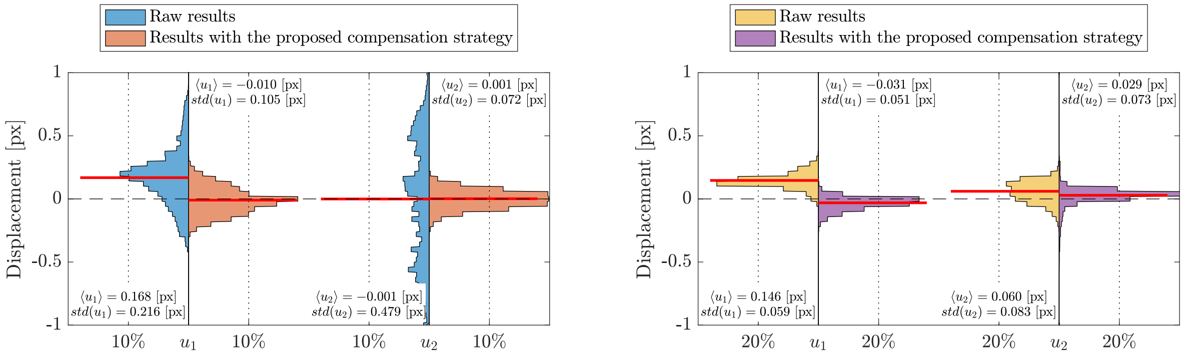

(a) Procedure A

(b) Procedure B

Figure 3: Validation of the proposed strategy, which corrects displacement measurements from camera movements. (a) is related to Procedure A, which focuses on measurement uncertainty due to machining table movements. (b) is related to Procedure B, which focuses on measurement uncertainty due to machining vibration. Note that data from pictures acquired when the cutting tool enters Block #2 are excluded. Indeed, tool entry into the material generates high-frequency vibrations, also inducing the measurement of high-frequency displacement fields (see Figure 4).

strategy strongly reduces this dispersion. These results lead us to assume that the proposed strategy correctly compensates for the measurement impairment due to uncontrolled camera movements associated with table movements.

- For procedure B, the observed displacement fields mainly resemble the one displayed in Figure 4(a). Nevertheless, some displacement fields correspond to the one of Figure 4(b). It is assumed that in this case, images were taken precisely when the tool enters Block #2. At these times, the observed workpiece, *i.e.* Block #1, but also the camera sensor are subjected to high dynamical loading. Figures 4(c) & (d) represent the measurements obtained with the proposed compensation strategy when applied on the same set of images as Figures 4(a) & (b). It is worth noting that this strategy also works well for the highly disturbed displacement field, since the mean values are closer to zero. Nevertheless, in the following, images corresponding to times where the cutting tool enters the material to be machined and thus in which the retrieved displacement maps feature high spatial heterogeneity as illustrated in Figure 4(b) & (d), are excluded from the uncertainty analysis.

The uncertainty analyses of the latter are presented in Figure 3(b). Yellow histograms are given for the raw measured displacements. Purple histograms correspond to the measurements obtained with the same set of images but when the proposed strategy compensating for camera movements is applied. As expected, the proposed strategy corrects the unwanted camera movements. This is confirmed by the high reduction in mean displacement values $\langle u_1 \rangle$ and $\langle u_2 \rangle$.

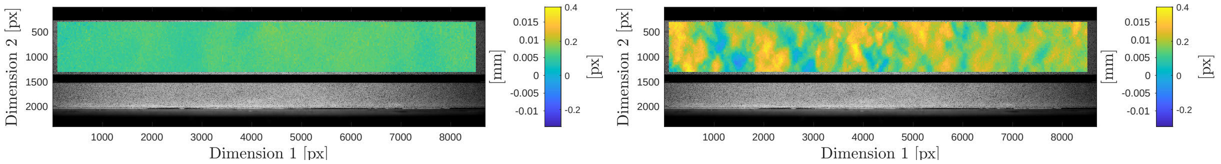

(a) raw results, $\langle u_2 \rangle = 0.124$ [px]

(b) raw results, $\langle u_2 \rangle = 0.184$ [px]

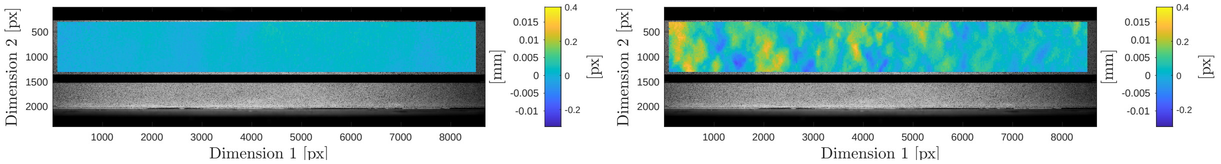

(c) with the proposed compensation strategy, $\langle u_2 \rangle = 0.009$ [px]

(d) with the proposed compensation strategy, $\langle u_2 \rangle = 0.062$ [px]

Figure 4: Observing Block #1 during the machining of Block #2. (a) & (c) are examples of retrieved displacement fields during machining. (a) corresponds to the raw measurement and (c) to the one offered with the proposed compensation strategy. (b) & (d) are the measurements obtained when the tool enters into Block #2. (b) corresponds to the raw measurement and (d) to the one offered with the proposed compensation strategy.

These both strategies ensure to conduct a first repeatability in the harsh environment of machining. Images represent indeed independent measurements of an identical material state. Error is in average about 0.03 [px] (approx. 1.5 [μm]) and its standard deviation about 0.1 [px] (approx. 5 [μm]).

This section revisited the original DIC formulation in order to introduce a method that compensates for uncontrolled camera movements. A study of measurement uncertainties validated this strategy. Nevertheless, the particularly harsh environment of machining requires further specification of the DIC algorithm to enable relevant full-field measurements. For instance flying metal chips also corrupt DIC measurements. The following section proposes a novel strategy to avoid such impairments.

2.2.3. Online DIC domain definition for measurement in the presence of metal chips

Machining and more specifically milling produces numerous metal chips. The DIC principle, as stated in Equation (2), relies on the conservation of the brightness. Flying metal chips corrupt this principle. This is illustrated in Figure 5. This is not, however, an issue for the Local version of DIC. Indeed, in the presence of metal chips, the minimization process diverges. No measurement is thus available at the metal chip location, as expected. Considering the global DIC version, its robustness appears here as a drawback. Due to the large support Ω_{rz} used for the displacement calculation, convergence is indeed still ensured when metal chips raise the field of view, but the resulting displacement field is consequently corrupted. The idea proposed here consists in redefining the domain Ω_{rz}^t, for each time t associated with each image $I_t(\underline{\mathsf{x}}_{\mathsf{p}})$, in order to exclude flying metal chips. The next paragraph details the elaboration of domain Ω_{rz}^t.

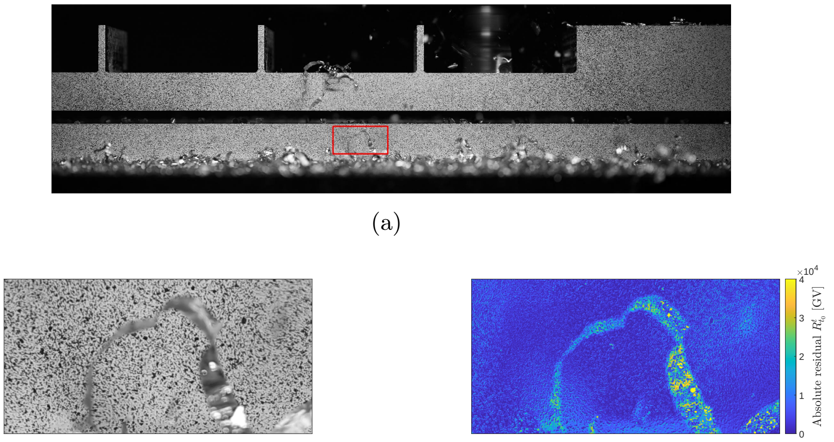

(a)

(b)

(c)

Figure 5: Photo of the observed workpiece during its machining. (a) image captured by the camera. (b) close-up corresponding to the red rectangle of (a). (c) absolute value of residual $R^t_{t_0}$, metal chips are evidently impairing the DIC principle: brightness is not conserved over time.

In practice, DIC minimization is performed through a modified Newton Raphson scheme. Residual $R^t_{t_0}$ is an excellent indicator of the validity of the brightness conservation hypothesis. It easily indicates whether the introduced kinematics are poorly defined or the DIC principle is not applicable. Figure 5(c) shows the absolute value of the residual map $R^t_{t_0}(\underline{\mathsf{x}}_{\mathsf{p}}, \underline{u})$, for the first iteration of the minimization scheme. This map is limited here to the red rectangular area defined in Figure 5(a), in which a metal chip is obviously present. As expected, the violation of the brightness conservation that this metal chip introduces is also clearly visible in the residual map. The proposed strategy for determining the domain Ω^t_{rz} relies thus on the residual map. Ω^t_{rz} is initialized to Ω_{rz}. Then, at each iteration, a smoothed residual map is computed by applying a moving average filter of width ℓ on the residual. This smoothing filter is introduced to avoid singularity results close to the metal chip contour. Ω^t_{rz} then gathers all pixels where the smoothed residual is below the threshold value R^{lim}. Several illustrations of threshold R^{lim} and width ℓ of the averaging filter are given in Figure 6. The white pixels of these residual maps correspond to the pixels removed from the initial domain Ω_{rz} to define Ω^t_{rz}. Experience shows that the parameters $R^{lim} = 5000$ and $\ell = 14$ [px] are conservative. They are used in what follows.

The proposed strategy for taking into account the flying metal chips is then validated by investigating the uncertainties of displacement measurements. 100 images of Block #1 are captured. The machining-tool was turned off, though metal chips were nevertheless manually projected into the camera's field of view. Using the same reference image, 99 mixed Global-Local DIC are performed to measure the displacement field of the imaged area of Block #1. Histograms of the displacement distributions are displayed in Figure 7 for raw and corrected measurements by reducing Ω_{rz} to

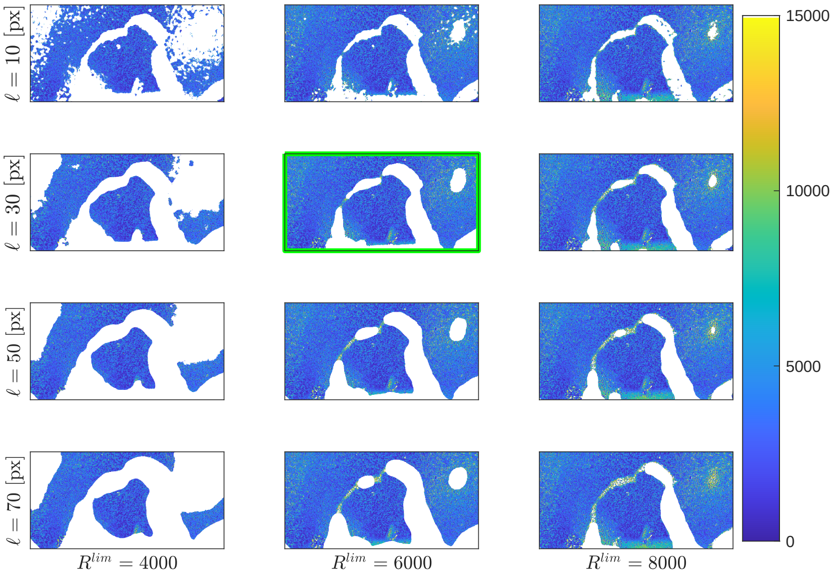

Figure 6: Illustrations of parameters R^{lim} and ℓ on the definition of Ω^t_{rz}. Pixels whose residual exceeds R^{lim} appear white on these maps. Only the area defined by the red rectangle in Figure 5(a) is represented. The set of parameters chosen in what follows is highlighted with a green border.

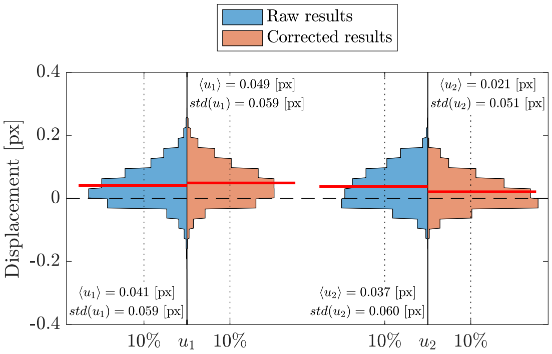

Figure 7: Displacement uncertainties: raw results and results obtained after the application of the metal chip-specific correcting filter to residual maps.

Ω^t_{rz}. The average displacement obtained with the correction is closer to zero, with a slightly more concentrated distribution.

This section proposed a time-dependent definition of the region of interest Ω^t_{rz}, on which the Global version of DIC relies for measuring the displacement due to camera movements. This online definition of the DIC integration domain avoids measurement impairment due to violation of brightness conservation, due here to flying metal chips. A study of measurement uncertainties validated the proposed strategy. Expected measurements feature a standard deviation of approximately 1/10 of a pixel, which corresponds here to 5 [μm]. In what follows, any DIC measurements are performed using the both strategies for taking into account unwanted camera movements along with flying metal chips. The harsh machining environment is thus controlled and reliable full-field measurements are possible.

3. Measurement of large workpiece behavior during machining

The goal of the proposed measurement tool is to provide the deformation of a workpiece during its machining. In its current version however, only in-plane displacements of planar surfaces are considered. This limits the shape of studied workpiece and the machining sequence. Nevertheless, these initial measurements provide a few observations of interest. The focus is thus made on analyses that (i) highlight the machining thermal influence during machining, (ii) validate the proposed tool thanks to a comparison with measurements provided by a traditional off-line measurement, (iii) quantify workpiece deformation due to machining forces and residual stresses, and finally (iv) illustrate the relevance of such instrumentation.

3.1. Geometry of the machined workpiece and machining sequences

The studied workpiece is presented in Figure 8. Figure 8(b) provides a 3D view and illustrates the so-called top and bottom sides. This geometry was chosen because it is representative of usual aeronautical parts. Pocket bases and thin walls, however, feature a greater thickness than conventional aeronautical structural parts. This thickness increase was chosen for two reasons. First, it still limits part vibrations during machining [1]. Moreover, the macro-effects of residual stress induced by cutting or of the cutting tool itself become negligible [15, 43]. Indeed, several works have been realized to measure and/or simulate the residual stress induced by cutting parameters and tool geometry in aluminium alloys [30]. However, in all these studies the affected depth stays below 250 [μm] [24]. Thus, as it is illustrated in Rambaud's work [30], it influence on part deflection can be neglected in our case since the minimum wall thickness is 4 [mm]. Finally, this geometry has demonstrated its relevance for the study of part deformation during machining due to residual stress in other studies [19, 13, 34]. Indeed, for this test part shape, expected displacements due to residual stress release are readily observable since they are in the order of approximately 0.1 [mm] during machining and a few millimeters when un-clamping the part.

The part is machined from a raw aluminum 7010 aluminum block of 886×100×100 [mm^3] supplied by Constellium. It is positioned and clamped on the machining table as shown in Figure 10(a). The part is secured with four clamps and three cylinders ensure part positioning on the machine-tool table.

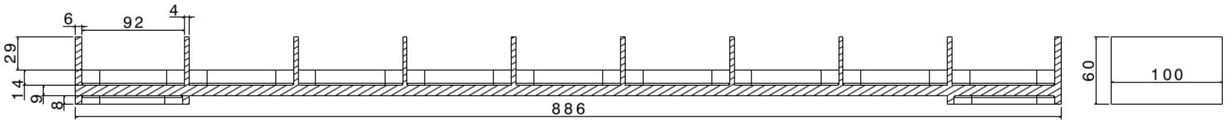

(a) workpiece geometry

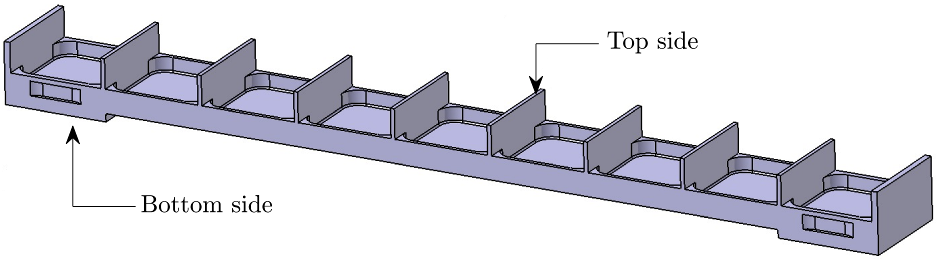

(b) 3D view

Figure 8: Objective geometry of the machined workpiece. Its slender design, obtained after removing 90% of the raw material, resembles the usual geometry of an aeronautical part.

Tool	Diameter mm	Z	V_C $(m.min^{-1})$	f_z $(mm.r^{-1}.teeth^{-1})$	V_f $(mm.min^{-1})$	a_p (mm)	N $(r.min^{-1})$
End-mill D32	32	3	1000	0.1	2984	2	9947
End-mill D100	100	6	1000	0.1	1911	1	3185

Table 1: Tools and cutting parameters: Z, number of teeth; V_c, cutting speed; f_z, feed rate per tooth; V_f, feed rate; a_p, depth of cut; N, spindle speed.

The cutting conditions used are summarized in Table 1. Two cutting tools are used, an end-mill of 32 [mm] diameter and an end-mill of 100 [mm] diameter. Tool details and cutting condition are given in Figure 9. The machining sequence consists of three stages, called "Phase 02", "Phase 10" and "Phase 20" and illustrated in Figure 10(b-d). Between each machining phase, the part is flipped upside down.

Detailed descriptions of the three phases are given in what follows:

- **Phase 02.** The first machining operation consists of a uniform 2 [mm] surface milling on the top side with end-mill D100 in order to obtain a planar surface consistent for part positioning

Figure 9: Tool details.

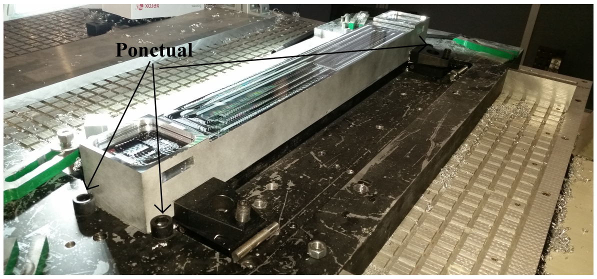

(a) Machining positioning

(b) Material removal performed in Phase 02

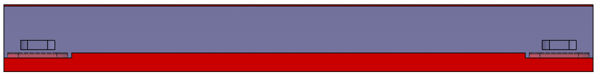

(c) Material removal performed in Phase 10

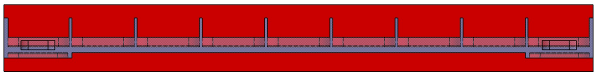

(d) Material removal performed in Phase 20

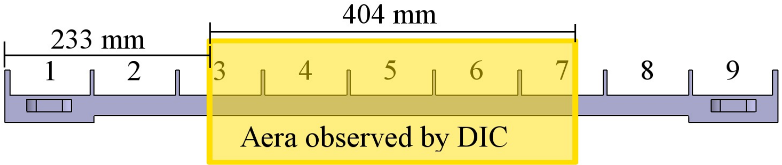

(e) Illustration of the machining sequencing. The yellow box corresponds to the camera field of view.

Figure 10: (a): Machining positioning is achieved with three point contacts. (b-d): illustrations of the machining performed during the three machining phases. Material removals are represented in red.

in phase 10.

- **Phase 10.** This phase consits of three machining operations, that generate the bottom side shape of the workpiece, as shown in Figure 8(b). The first operation consists of a uniform 20 [mm] surfacing with end-mill D100. The notches dedicated to the clamping for Phase 20 are then machined using a face and side milling cutter. The final operation consists in machining two closed pockets at both ends of the part, along with a large open central pocket with end-mill D32. The geometry shown in figure 10(c) is obtained.

- **Phase 20.** Clamping is performed with four clamps, which apply a pressure on notches previously machined in the workpiece. A torque wrench is used to apply a torque of 60 [N.m] to each load screw. Phase 20 comprises two milling operations. The first one consists in surfacing 18 [mm] of the top side of the workpiece with end-mill D100, as shown in Figure 8(a). After this operation, the workpiece reaches the desired height of 60 [mm]. The second and last machining operation consists in milling the 9 pockets of 43 [mm] depth with end-mill D32. Each pocket consists of two sub-pockets; the upper sub-pocket is a 29 [mm] open pocket and the bottom sub-pocket is a 14 [mm] closed pocket. The final geometry shown in Figure 8(b) is obtained. The pocket machining sequence is indicated in Figure 10(e). During the final passes of each closed pocket, the depth of cut is first reduced to 1.5 [mm], then to 1 [mm] when vibration phenomena appear. The camera's field of view is also depicted in Figure 10(e).

DIC relies on the comparison of two images to retrieve the displacement field that differentiates them. The resulting displacement is consequently defined relative to a reference image. The whole machining, clamping and un-clamping sequences are thus observed with DIC in order to accurately compute the displacement field at each moment. The image acquisition frequency is 0.2 [Hz]. It is worth noting that to perform this DIC measurement, lubrication is not possible. Consequently, the part heats up during machining. In order to limit the impact of the thermal expansion phenomenon, delays are implemented after each surfacing and pocketing operation. The image acquisition frequency is reduced to 1/30 [Hz] during these cooling periods. Approximately 2000 images are acquired during one complete part machining operation.

3.2. Measurement of ahick workpiece behavior during surface machining

Lubrication is here not performed, in order to limit the masking of the observed surface by the camera. This was taken into account for setting up cutting parameters. Nevertheless, the heat generated by machining is not dissipated and this leads to an increase in workpiece temperature, which in turn induces isotropic expansion. This is particularly true when the machining operation removes material over a significant length of the workpiece, as during the first surfacing operation of each phase. Thermal expansion is observed and studied for the first machining stage of Phase 20. This initial study presents the kind of results obtained with our developed *in-situ* measurement method. Four images are taken at times t_0, t_1, t_2, and t_3. The corresponding times are defined in Table 2. Four DIC field measurements are computed, denoted $\underline{u}_{t0}^{t1}$, $\underline{u}_{t0}^{t2}$, $\underline{u}_{t0}^{t2}$ and $\underline{u}_{t2}^{t3}$. Note that $\underline{u}_{t_a}^{t_b}$ is the displacement field between times t_a and t_b. These displacement fields are shown in Figure 11.

t_0	Initial time (unclamped raw part).
t_1	Start of Phase 20, after clamping. Phase 02 and Phase 10 already realized.
t_2	End of the first 18 [mm] deep surfacing of Phase 20.
t_3	$t_3 = t_2 + \Delta t$, with Δt equal to 20 [min]. No machining has been performed during Δt.

Table 2: Definitions of times t_0, t_1, t_2 and t_3.

This gives rise to a few observations:

- The order of magnitude of the displacement maps is higher than the uncertainties. The preceding section concluded that the standard deviation of the measurement is approximately 0.1 [px]. This is below the spatial distribution of the retrieved displacements. When considering a small region of interest, as illustrated in Figure 11(e), heterogeneities in the displacement fields are related to noise propagation, from images to displacement fields or are due to the pattern itself [7, 8, 38, 39]. Observed measurements are thus in their confidence range and correspond to workpiece surface deformation. We can thus use this measurement of displacement fields to analyze part behavior.

- Figure 11(b) displays the horizontal (left-hand side) and vertical (right-hand side) displacements of the observed surface at time t_1, *i.e.* after the clamping of the workpiece for Phase 20 (beginning of Phase 20). Thus, the measured displacement $\underline{u}_{t_0}^{t_1}$ is due to the machining operations performed during Phase 02 and Phase 10, and to the clamping operations.

  Between times t_0 and t_1, the workpiece was clamped three times and un-clamped twice. Such workpiece movements mainly explain the measured horizontal displacement. Workpiece bending by more than 0.1 [mm] is also observed. This is the consequence of the residual stress release due to the 20 [mm] thick material removal of Phase 10. It explains the measured vertical displacement values which are near 20 [mm] due to a Phase 20 part positioning on the Phase 10 machining plans at the two ends of the workpiece.

- Figure 11(c) shows the complete displacement $\underline{u}_{t_0}^{t_2}$ of the workpiece from initial time t_0 to the first 18 [mm] machining operation of Phase 20. This is the first machining operation of Phase 20.

  In the measured field, we observed two phenomena. The slender geometry of the workpiece ensures the separation of these two phenomena. The first one concerns the residual stress release due to material removal by machining. This mainly affects the vertical component of the displacement (right-hand side of Figure 11(c)), which consequently slightly unbends in this machining case. Machining also generates heat that warms up the workpiece. Consequently, this latter expands. Due to the particular geometry of the workpiece, this is observable in the horizontal component of the displacement field (left-hand side of Figure 11(c)). In this figure, we can see that the workpiece homogeneously deforms until 0.3 [mm].

- A delay of 20 [min] is introduced to observe the displacement due to the thermal cooling of the workpiece. Figure 11(c) shows complete displacement $\underline{u}_{t_0}^{t_3}$ of the workpiece after this thermal release. The color scales of horizontal and vertical displacement maps, resp. left-hand and right-hand sides, are identical to the Figure 11(b). This allows us to focus on the disappearance of the kinematic expansion associated with the cut-off of thermal heating.

This is highlighted in Figure 11(d), which shows only incremental displacement $\underline{u}_{t_2}^{t_3}$ due to workpiece cooling from t_2 to t_3. Because of the machining positioning elements, which are on the right side, thermal expansion stretches the workpiece to the left side (left-hand side of Figure 11(d)). Displacements related to the thermal release of the workpiece correspond to relatively homogeneous strain spatial distribution. This was expected because of the large surface that has been machined and the workpiece geometry.

This initial analysis of the results provided by this *in-situ* measurement method validates the relevance of the measured displacement field during machining. In the following section, an analysis of part deformation after machining is conducted to validate the results obtained.

3.3. Measurement of final geometrical features - validation of the DIC measurement tool

The *in-situ* and contactless measurement technique is validated by comparing the estimated final machined workpiece geometry after unclamping with a measured one, obtained by probing using a Coordinate Measuring Machine (CMM).

The vertical positions of the bottom surface of each pocket are estimated by DIC or measured by CMM. Figure 12 illustrates the vertical positioning error that is deduced with these two measurement tools. DIC measurements rely here on two cameras. Camera #1 is the same as the one studied until now. An extra one, denoted here Camera #2 has been added to extend the workpiece observation window to the left-end front clamp. There are no DIC measurements for $x_1 \in [20, 50]$ [mm] as the clamp hides the workpiece surface. Camera #2 is a Nikon D3, featuring a 12 Megapixels CMOS sensor, equipped with a Nikkor 105 [mm] lens. The same table movement and metal chip compensation strategies are implemented. For each pocket, the DIC estimation of its position is based on the comparison of the reference image, defined by an image of the raw workpiece, with the last available image taken during pocket milling. The position of a bottom pocket combines this estimation when the workpiece is clamped with the final displacement of the unclamped workpiece. Because the positions of 7 pockets are presented in Figure 12, it thus summarizes 7 different DIC measurements. These results show a relatively good agreement between *in-situ* DIC measurements and *offline* probing measurements. This agreement validates the *in-situ* DIC measurement tool.

3.4. Workpiece deflection due to machining forces

The proposed DIC measurement tool is used in this section to perform *in-situ* measurements. This first analysis is used in particular to study the effect of milling force on workpiece deformation. For this purpose, DIC compares an image taken at time t_b, corresponding to the instant immediately

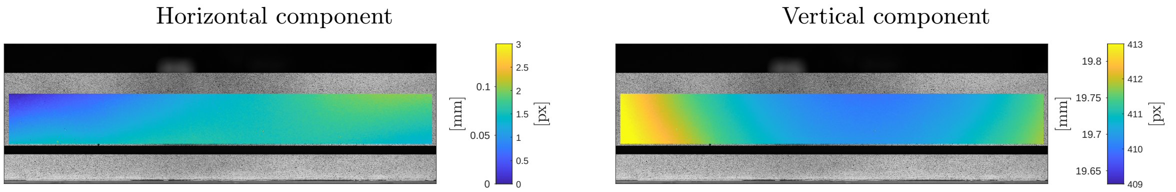

(a) $\underline{u}_{t_0}^{t_1}$, with t_1 corresponding to the beginning of Phase 20.

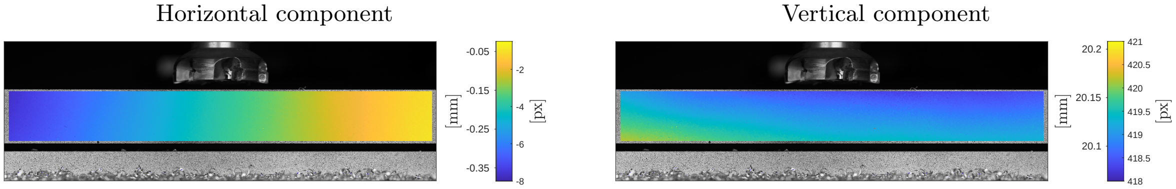

(b) $\underline{u}_{t_0}^{t_2}$, with t_2 corresponding to the end of first 18 [mm] surface machining of Phase 20.

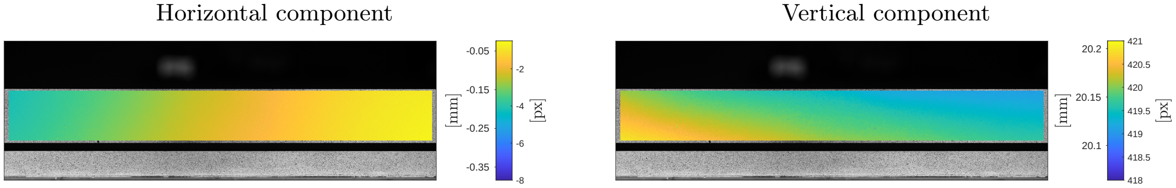

(c) $\underline{u}_{t_0}^{t_3}$, with $t_3 = t_2 + 20$ [min].

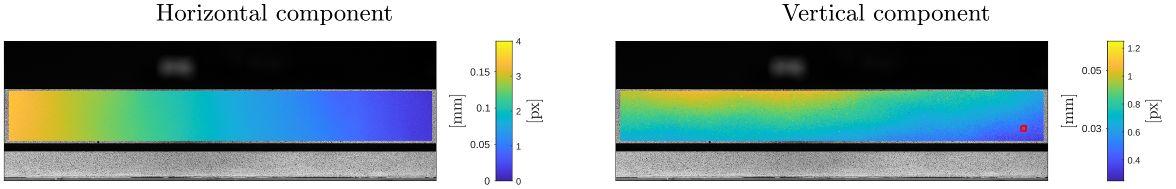

(d) $\underline{u}_{t_2}^{t_3}$ corresponding to the cooling effect

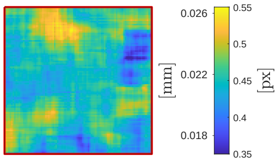

(e) Close-up of ${u_2}_{t_2}^{t_3}$, at the red box location.

Figure 11: Observation of the first machining operation of Phase 20. See Figure 2 for the first picture of the machining, which thus describes the initial state, at time t_0. Grey value images, which are used in the background here, are the current images used for each DIC measurement. Material was removed during Phase 10 on the bottom of the workpiece from t_0 to t_1. From t_1 to t_2, the first material removal of 18 [mm] of Phase 20 was performed on the top side. (e) illustrates the spatial distribution of the results in the small red box plotted in the right-hand side on (d). This distribution shows the order of magnitude of the measurement uncertainty.

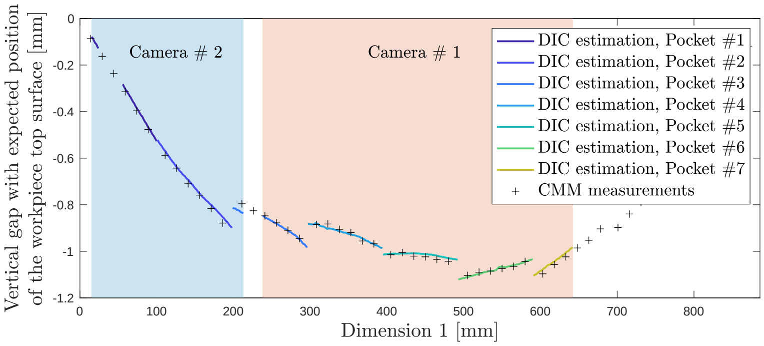

Figure 12: Focus on the position of the top surfaces of the workpiece: gap between expected and measured positions. Measurements are performed with a conventional probing CMM (black crosses) or estimated thanks to DIC measurement during workpiece machining (lines).

after the pocket is finished and when the tool is out of the material, with the one taken at time t_a at the end of pocket machining operation when the tool is still removing material, $t_b > t_a$. The machining of Pocket #5 is studied here. The displacement field between these two times is illustrated in Figure 13 showing horizontal and vertical component of displacement $\underline{u}_{t_b}^{t_a}$ and an illustration of part displacement as a magnified deformed mesh. The magnification factor here is 150.

These DIC measurement means serve to measure part deflection due to cutting forces. In this studied case, the maximum measurement vertical displacement value is near 0.05 [mm]. Thus, this *in-situ* measurement allows the collection of information about the macro-interaction between tool and workpiece.

3.5. Full-field measurements during machining - studying the workpiece behavior

The proposed DIC measurement tool is also used to observe workpiece deflection during machining. Such observations are useful for the validation of the numerical simulations that propose predictions of workpiece deflection due to residual stress. Here, images are thus regularly taken and DIC applied to them. The focus is on Phase 20 during the pocketing operations, when the tool is out of the material and the considered reference image depicts the workpiece before clamping. Results are shown in Figure 14(a). Such fields would perfectly feed an inverse method, for instance the Finite Element Updating Method, to estimate the initial residual stress distribution.

The workpiece is maintained clamped throughout the machining sequence. Consequently, the observed displacements are strictly induced by the removal of material and the milling process. It corresponds to thermal heating of the workpiece and to its elastic response after the release of residual stress. To minimize the thermal effect a delay Δt, as discussed in Section 3.2, was allowed at the end of each pocket milling before taking the corresponding photo. This effect is omitted in what follows.

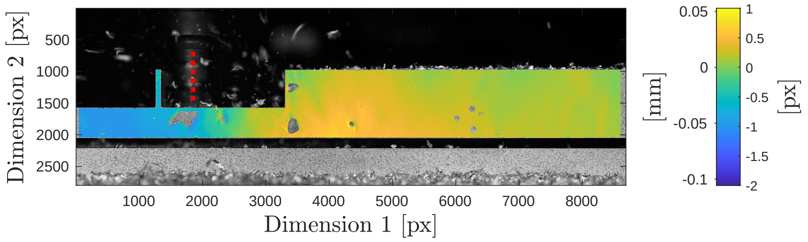

(a) Horizontal component

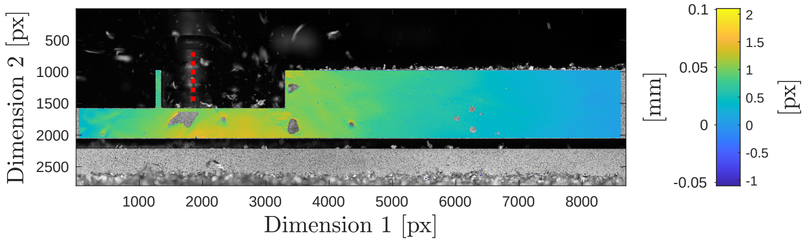

(b) Vertical component

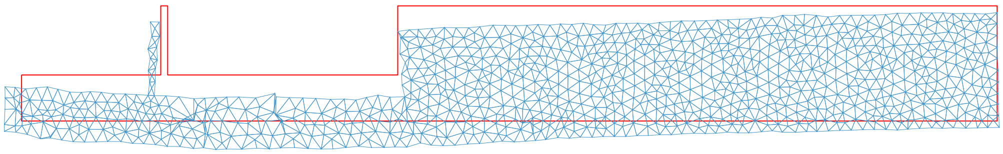

(c) Illustration of the displacement field represented as a magnified deformed mesh (magnification = 150)

Figure 13: Displacement fields $u_{t_b}^{t_a}$ due to milling forces. DIC is inversely applied here on two consecutive images. The reference image, taken at time t_b, corresponds here to the first image taken once Pocket #5 is finished. The current image, taken at time t_a, is the last one imaging the milling of this pocket. (a) and (b) respectively show the horizontal and vertical displacements, on top of the considered current. An illustration of this displacement field is provided in (c), where a mesh is deformed with the displacement, magnified 150 times.

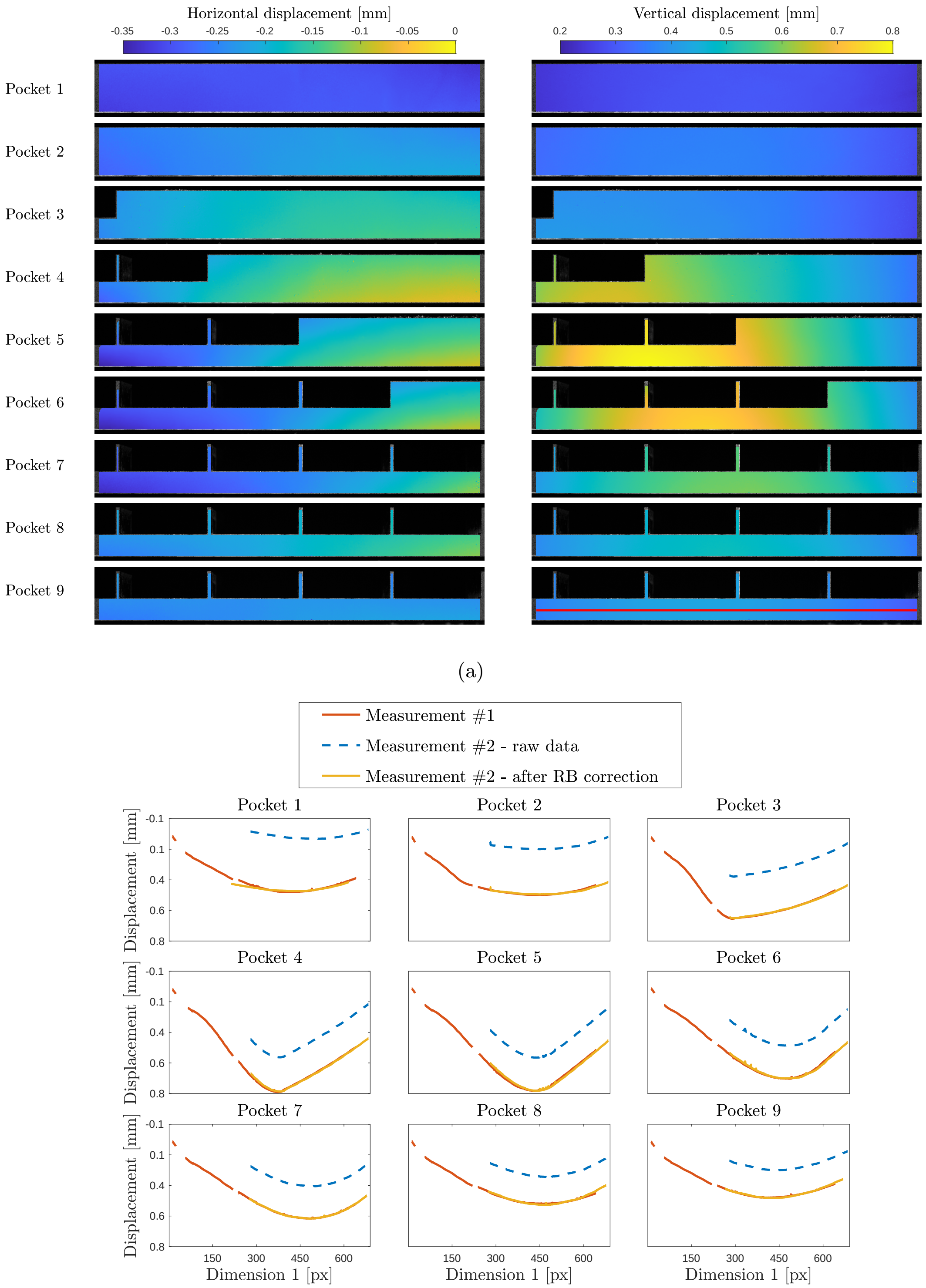

(a)

(b)

Figure 14: (a) Horizontal component (left-hand side) and Vertical component (right-hand side) of the displacement measured at the end of the machining of each pocket. The red line plotted on the ninth pocket maps shows the position of the extracted displacements used for figure (b). Note the inverse direction of the y-axis, which has been chosen for clarity and to remain consistent with the reference system of the problem (see Figure 2).

The largest displacements are observed once half of the machining sequence has been performed. Because the pockets are machined one after the other, the middle of the machining sequence coincides with the time when the workpiece is the least symmetrical. The flexure stiffness of the workpiece is thus less homogeneous at this time, and the displacements reflect this singularity. The retrieved displacements reveal a beam-like behavior of the workpiece, which is mainly explained by its beam-like geometry. Despite their richness, full-field maps are difficult to interpret. For this purpose, the workpiece is considered as a beam and the measured displacement fields serve to infer its movement during machining. The considered neutral fiber is defined as the middle line of the unmachined part of the bottom of the workpiece. This line is plotted in Figure 14(a) for the ninth pocket. For noise reduction, line displacement is computed on a ±50 pixel vertical band width. Results are illustrated in Figure 14(b). Measurement #1 is depicted with the red line. It consists of the preceding full-map results, but reduced to the neutral fiber displacement and completed with the measurements obtained thanks to the use of the extra camera #2 as in Section 3.3. The measurements of a second machining workpiece, identical to the one described until now, were also performed for validation purposes. This second machining is denoted here as Measurement #2 in Figure 14(b). The raw measurement directly given by the DIC tool is the blue dashed line. A solid rigid movement occurs between the workpiece and the machining table, certainly due to mispositioning of the workpiece prior to clamping. A simple translation of the results has been introduced, giving the yellow line. The displacement observed for this second machining is finally in excellent agreement with the one corresponding to the first machining.

Since the reference image captures the workpiece before clamping, the retrieved displacements sum the effects of the clamping, of the first 18 [mm] surfacing and of the pocket milling. The focus is first made on the removal of 20 [mm] material on the bottom surface of the workpiece during Phase 10. Once unclamped, the workpiece bent. Because Phase 20 processes the top surface of the workpiece, this latter is flipped upside down and clamped once more. This last clamping forces the workpiece to deform and induces an initial displacement of the workpiece, which is then observable at the end of the first pocketing in Figure 14(b). The clamping system constrains a small area of the workpiece bottom, and consequently a slight vertical displacement is observed above the clamping system. The analysis of these measurements allows the determination of undercut or overcut during machining, which are mainly due to the residual stress release. Such a study thus allows to choose a machining sequence to be chosen with regard to the expected accuracy of the final workpiece geometry.

4. Conclusion

Machining community calls for a better instrumentation of the machining tool. Multiple phenomena occur during material removal and machined workpiece deforms during machining operation, and does not satisfy the expected geometry constraints. In this paper, the DIC technique, widely used in the experimental mechanics community, has been generalized to the harsh context of machining. A new *in-situ* DIC measurement tool is indeed proposed to quantify the deformation of a workpiece during its machining. The main advantages of the proposed tool consist in its contactless feature and the fact that it provides full-field maps.

In order to ensure consistent measurements in the unusual environment of machining, a numerical compensation of camera movement and chip filtering is developed. These approaches are validated thanks to a thorough study of measurement uncertainty. Expected measurements feature a standard deviation approximately $1/10^{\text{th}}$ of a pixel, which corresponds here to 5 [μm]. Moreover, two identical machining sequences are measured and are in excellent agreement.

The measurement tool is then implemented to analyze workpiece behavior during machining. Various phenomena are observed and discussed, such as thermal expansion, residual stress release or workpiece deformation due to machining force. The outputs offered by this measurement tool provide the experimentalist with new perspective to assess workpiece position during machining. The perspectives of such a tool are numerous. Amongst others, it greatly facilitates the numerical-experimental dialogue required for characterization purposes or simply as validation of numerical prediction of workpiece deformation during machining. Further work will extend this 2D measurement tool to 3D.

Acknowledgements

This work benefited from the support of the project SIMP-AERO N° ANR-15-CE10-0005-01 of the French National Research Agency (ANR).

This work was carried out within the Manufacturing 21 working group, which comprises 15 French research laboratories. The topics covered are the modeling of the manufacturing processes, virtual machining, and the emergence of new manufacturing methods.

B. Blaysat is grateful to the French government research program “Investissements d’Avenir” for their financial support (IDEX-ISITE initiative 16-IDEX-0001, CAP 20-25).

References

[1] Altintas, Y. and Budak, E. (1995). Analytical prediction of stability lobes in milling. *CIRP Annals-Manufacturing Technology*, 44(1):357–362.

[2] Arriola, I., Whitenton, E., Heigel, J., and Arrazola, P. J. (2011). Relationship between machinability index and in-process parameters during orthogonal cutting of steels. *CIRP Annals-Manufacturing Technology*, 60(1):93–96.

[3] Aurrekoetxea, M., López de Lacalle, L. N., and Llanos, I. (2020). Machining stresses and initial geometry on bulk residual stresses characterization by on-machine layer removal. *Materials*, 13(6).

[4] Baizeau, T., Campocasso, S., Rossi, F., Poulachon, G., and Hild, F. (2016). Cutting force sensor based on digital image correlation for segmented chip formation analysis. *Journal of Materials Processing Technology*, 238:466–473.

[5] Bay, B., Smith, T., Fyhrie, D., and Saad, M. (1999). Digital volume correlation: three-dimensional strain mapping using X-ray tomography. *Experimental Mechanics*, 39(3):217–226.

[6] Besnard, G., Hild, F., and Roux, S. (2006). “Finite-element” displacement fields analysis from digital images: application to Portevin–Le Châtelier bands. *Experimental Mechanics*, 46(6):789–803.

[7] Blaysat, B., Grédiac, M., and Sur, F. (2016a). Effect of interpolation on noise propagation from images to DIC displacement maps. *International Journal for Numerical Methods in Engineering*, 108(3):213–232.

[8] Blaysat, B., Grédiac, M., and Sur, F. (2016b). On the propagation of camera sensor noise to displacement maps obtained by DIC - an experimental study. *Experimental Mechanics*, 56(6):919–944.

[9] Blaysat, B., Hoefnagels, J. P. M., Lubineau, G., Alfano, M., and Geers, M. G. D. (2015). Interface debonding characterization by image correlation integrated with Double Cantilever Beam kinematics. *International Journal of Solids and Structures*, 55:79–91.

[10] Bowden, D. M. and Halley, J. E. (2001). Aluminium reliability improvement program final report 60606. Technical report, The Boeing Company: Chicago, IL, USA.

[11] Cerutti, X. and Mocellin, K. (2015). Parallel finite element tool to predict distortion induced by initial residual stresses during machining of aeronautical parts. *International Journal of Material Forming*, 8:255–268.

[12] Cerutti, X., Mocellin, K., Hassini, S., Blaysat, B., and Duc, E. (2016). Methodology for aluminium part machining quality improvement considering mechanical properties and process conditions. *{CIRP} Journal of Manufacturing Science and Technology.*

[13] Cerutti, X., Mocellin, K., Hassini, S., Blaysat, B., and Duc, E. (2017). Methodology for aluminium part machining quality improvement considering mechanical properties and process conditions. *CIRP Journal of Manufacturing Science and Technology*, 18(18–38).

[14] Das, S. and Chandra, U. (1999). Residual Stress and Distortion. In Totten, G. and Mackenzie, D., editors, *Handbook of Aluminum Metallurgy: Processes and Equipment, vol. 1.* Marcel dek edition.

[15] Fuh, K.-H. and Wu, C.-F. (1995). A residual-stress model for the milling of aluminum alloy (2014-T6). *Journal of Materials Processing Technology*, 51(1-4):87–105.

[16] Ghadbeigi, H., Bradbury, S. R., Pinna, C., and Yates, J. R. (2008). Determination of micro-scale plastic strain caused by orthogonal cutting. *International Journal of Machine Tools and Manufacture*, 48(2):228–235.

[17] Grédiac, M., Blaysat, B., and Sur, F. (2017). A critical comparison of some metrological parameters characterizing Local Digital Image Correlation and Grid Method. *Experimental Mechanics*, 57(6):871–903.

[18] Grédiac, M. and Hild, F. (2013). *Full-field measurements and identification in solid mechanics.* Wiley Online Library.

[19] Hassini, S. (2015). *Qualification multi-critères des gammes d'usinage : application aux pièces de structure aéronautique en alliage Airware®*. PhD thesis.

[20] Hijazi, A. and Madhavan, V. (2008). A novel ultra-high speed camera for digital image processing applications. *Measurement Science and Technology*, 19(8):85503.

[21] Jeanmart, P. and Bouvaist, J. (1985). Finite element calculation and measurement of thermal stresses in quenched plates of high–strength 7075 aluminium alloy. *Materials Science and Technology*, 1(10):765–769.

[22] List, G., Sutter, G., Bi, X. F., Molinari, A., and Bouthiche, A. (2013). Strain, strain rate and velocity fields determination at very high cutting speed. *Journal of Materials Processing Technology*, 213(5):693–699.

[23] Llanos, I., Aurrekoetxea, M., Agirre, A., de Lacalle, L. N. L., and Zelaieta, O. (2019). On-machine characterization of bulk residual stresses on machining blanks. *Procedia CIRP*, 82:406–410.

[24] Madariaga, A., Perez, I., Arrazola, P. J., Sanchez, R., Ruiz, J. J., and Rubio, F. J. (2018). Reduction of distortions in large aluminium parts by controlling machining-induced residual stresses. *The International Journal of Advanced Manufacturing Technology*, 97(1):967–978.

[25] Moulart, R. (2007). *Développement et mise en oeuvre d'une méthode de mesure de champs de déformation à l'échelle micrométrique.* PhD thesis, Arts et Métiers ParisTech.

[26] Passieux, J.-C. and Bouclier, R. (2019). Classic and Inverse Compositional Gauss-Newton in Global DIC. *International Journal for Numerical Methods in Engineering*, page In Press.

[27] Pottier, T., Germain, G., Calamaz, M., Morel, A., and Coupard, D. (2014). Sub-millimeter measurement of finite strains at cutting tool tip vicinity. *Experimental Mechanics*, 54(6):1031–1042.

[28] Pujana, J., Arrazola, P. J., and Villar, J. A. (2008). In-process high-speed photography applied to orthogonal turning. *Journal of materials processing technology*, 202(1):475–485.

[29] Rai, J. K. and Xirouchakis, P. (2008). Finite element method based machining simulation environment for analyzing part errors induced during milling of thin-walled components. *International Journal of Machine Tools and Manufacture*, 48(6):629–643.

[30] Rambaud, P. (2019). *Computational modelling of post machining distortions of aluminium aeronautical parts : application to thin walls.* PhD thesis, Université PSL.

[31] Ramesh, R., Mannan, M., and Poo, A. (2000a). Error compensation in machine tools — a review: Part i: geometric, cutting-force induced and fixture-dependent errors. *International Journal of Machine Tools and Manufacture*, 40(9):1235–1256.

[32] Ramesh, R., Mannan, M., and Poo, A. (2000b). Error compensation in machine tools — a review: Part ii: thermal errors. *International Journal of Machine Tools and Manufacture*, 40(9):1257–1284.

[33] Rebergue, G., Blaysat, B., Chanal, H., and Duc, E. (2018a). Advanced DIC for accurate part deflection measurement in a machining environment. *Journal of Manufacturing Processes*, 33:10–23.

[34] Rebergue, G., Blaysat, B., Chanal, H., and Duc, E. (2018b). Advanced DIC for accurate part deflection measurement in a machining environment. *Journal of Manufacturing Processes*, 33:10 – 23.

[35] Réthoré, J. (2010). A fully integrated noise robust strategy for the identification of constitutive laws from digital images. *International Journal for Numerical Methods in Engineering*, 84(6):631–660.

[36] Réthoré, J., Hild, F., and Roux, S. (2008). Extended digital image correlation with crack shape optimization. *International Journal for Numerical Methods in Engineering*, 73(2):248–272.

[37] Schreier, H. W. and Sutton, M. A. (2002). Systematic errors in digital image correlation due to undermatched subset shape functions. *Experimental Mechanics*, 42(3):303–310.

[38] Sur, F., Blaysat, B., and Grédiac, M. (2020). On biases in displacement estimation for image registration, with a focus on Photomechanics - Extended version. Research report, LORIA (Université de Lorraine, CNRS, INRIA) ; Institut Pascal (Université Clermont-Auvergne, SIGMA, CNRS).

[39] Sur, F., Blaysat, B., and Grédiac, M. (Available online). On biases in displacement estimation for image registration, with a focus on Photomechanics. *Journal of Mathematical Imaging and Vision*.

[40] Sutter, G. (2005). Chip geometries during high-speed machining for orthogonal cutting conditions. *International Journal of Machine Tools and Manufacture*, 45(6):719–726.

[41] Sutton, M. A., Mingqi, C., Peters, W. H., Chao, Y. J., and McNeill, S. R. (1986). Application of an optimized digital correlation method to planar deformation analysis. *Image and Vision Computing*, 4(3):143–150.

[42] Tandon, R. and Green, D. J. (1990). Residual stress determination using strain gage measurements. *Journal of the American Ceramic Society*, 73(9):2628–2633.

[43] Tang, Z. T., Liu, Z. Q., Pan, Y. Z., Wan, Y., and Ai, X. (2009). The influence of tool flank wear on residual stresses induced by milling aluminum alloy. *Journal of Materials Processing Technology*, 209(9):4502–4508.

[44] Toubhans, B., Fromentin, G., Viprey, F., Karaouni, H., and Dorlin, T. (2020). Machinability of inconel 718 during turning: Cutting force model considering tool wear, influence on surface integrity. *Journal of Materials Processing Technology*, 285:116809.

[45] Van Beeck, J., Neggers, J., Schreurs, P. J. G., Hoefnagels, J. P. M., and Geers, M. G. D. (2014). Quantification of three-dimensional surface deformation using global digital image correlation. *Experimental Mechanics*, 54(4):557–570.

[46] Vendroux, G. and Knauss, W. G. (1998a). Submicron deformation field measurements: Part 1. Developing a digital scanning tunneling microscope. *Experimental Mechanics*, 38(1):18–23.

[47] Vendroux, G. and Knauss, W. G. (1998b). Submicron deformation field measurements: Part 2. Improved digital image correlation. *Experimental Mechanics*, 38(2):86–92.

[48] Virkar, A. V. (1990). Determination of residual stress profile using a strain gage technique. *Journal of the American Ceramic Society*, 73(7):2100–2102.

[49] Wang, Z. J., Chen, W. Y., Zhang, Y. D., Chen, Z. T., and Liu, Q. (2005). Study on the Machining Distortion of Thin-walled Part Caused by Redistribution of Residual Stress. *Chinese Journal of Aeronautics*, 18(2):175–179.

[50] Wei, Y. and Wang, X. W. (2007). Computer simulation and experimental study of machining deflection due to original residual stress of aerospace thin-walled parts. *The International Journal of Advanced Manufacturing Technology*, 33(3):260–265.

[51] Xu, H., Lu, M., Avila, J. R. S., and Qian, Z. (2019). Imaging a weld cross-section using a novel frequency feature in multi-frequency eddy current testing. *Insight - Non-Destructive Testing and Condition Monitoring*, 61(12):738–743.

[52] Zhang, D., Zhang, X.-M., Xu, W.-J., and Ding, H. (2017). Stress field analysis in orthogonal cutting process using digital image correlation technique. *Journal of Manufacturing Science and Engineering*, 139(3):31001.